

Northward Propagation Mechanisms of the Boreal Summer Intraseasonal Oscillation in the ERA-Interim and SP-CCSM

CHARLOTTE A. DEMOTT

Department of Atmospheric Science, Colorado State University, Fort Collins, Colorado

CRISTIANA STAN

*Department of Atmospheric, Oceanic and Earth Sciences, George Mason University, Fairfax, Virginia, and
Center for Ocean–Land–Atmosphere Studies, Calverton, Maryland*

DAVID A. RANDALL

Department of Atmospheric Science, Colorado State University, Fort Collins, Colorado

(Manuscript received 5 April 2012, in final form 19 September 2012)

ABSTRACT

Mechanisms for the northward propagation (NP) of the boreal summer intraseasonal oscillation (BSISO) and associated Asian summer monsoon (ASM) are investigated using data from the interim ECMWF Re-Analysis (ERA-Interim, herein called ERAI) and the superparameterized Community Climate System Model (SP-CCSM). Analyzed mechanisms are 1) destabilization of the lower troposphere by sea surface temperature anomalies, 2) boundary layer moisture advection, and boundary layer convergence associated with 3) SST gradients and 4) barotropic vorticity anomalies. Mechanism indices are regressed onto filtered OLR anomaly time series to study their relationships to the intraseasonal oscillation (ISO) and to equatorial Rossby (ER) waves.

Northward propagation in ERAI and SP-CCSM is promoted by several mechanisms, but is dominated by boundary layer moisture advection and the barotropic vorticity effect. SST-linked mechanisms are of secondary importance but are nonnegligible. The magnitudes of NP mechanisms vary from the Indian Ocean to the west Pacific Ocean, implying that NP is accomplished by different mechanisms across the study area.

SP-CCSM correctly simulates observed NP mechanisms over most of the ASM domain except in the Arabian Sea during the early stages of the monsoon life cycle. Reduced NP in the Arabian Sea arises from weaker-than-observed easterly shear, reducing the effectiveness of the barotropic vorticity mechanism. The ability of SP-CCSM to correctly simulate NP mechanisms in other regions results from the model's ability to simulate reasonable mean wind and moisture fields, a realistic spectrum of variability, and the capability of convection to respond to boundary layer changes induced by large-scale NP mechanisms.

1. Introduction

The 30–50-day intraseasonal oscillation (ISO) is one of the dominant modes of tropical variability during boreal winter and summer seasons. In boreal winter the ISO is also known as the Madden–Julian oscillation (MJO) (Madden and Julian 1971) and is characterized by a large-scale, equatorially confined convective

envelope and associated zonal circulation system that propagates eastward at $\sim 5 \text{ m s}^{-1}$ (Madden and Julian 1972; Zhang 2005). The ISO during boreal summer is more complex than the winter season counterpart, exhibiting northward- and westward-propagating modes in addition to the underlying MJO eastward propagation. Northward propagation, which occurs on ISO time scales, originates near the equator and extends to $\sim 20^\circ\text{N}$, and contributes to monsoon rain onset and break periods over India, Southeast Asia, and the western North Pacific Ocean. The northward-propagating ISO (NPISO) commences with the development of low-level southwesterly monsoon flow in May–June. The NPISO, which may or

Corresponding author address: Charlotte A. DeMott, Department of Atmospheric Science, Colorado State University, Fort Collins, CO 80523.

E-mail: demott@atmos.colostate.edu

may not be associated with the eastward-propagating MJO (Wang and Rui 1990; Lawrence and Webster 2002), may result from internal atmospheric dynamic processes (e.g., Wang and Xie 1997; Jiang et al. 2004; Bellon and Sobel 2008) and/or anomalous surface fluxes in cloud-free regions north of existing convection (e.g., Webster 1983; Fu et al. 2003; Klingaman et al. 2008b).

Historically, dynamic theories for northward propagation (NP) mechanisms focus on the interaction of tropical convection and the deep easterly zonal shear that develops as a consequence of the seasonal low-level wind shift over the Indian Ocean and west Pacific Ocean. The role of equatorial Rossby (ER) waves in monsoon NP was first noted by Lau and Peng (1990). Using a hydrostatic two-level equatorial beta-plane model, Wang and Xie (1996) and Xie and Wang (1996) described the interaction of ER waves with deep easterly shear and attributed NP to the coupling of baroclinic and barotropic components of equatorial wave motions, with the barotropic component emanating northward. Using a three-dimensional intermediate model, Wang and Xie (1997) demonstrated the relationship between an eastward-propagating Kelvin–Rossby wave packet and NP, which led to the concept of the monsoon as a “tilted rainband.” For MJO-linked convective events, the combination of the eastward-moving MJO and northwestward-moving ER wave produces a northwest–southeast-tilted rainband that translates eastward. To an observer at a fixed point, eastward passage of this tilted rainband appears as a northward-propagating convection front.

The dynamic nature of NP and its governing processes continued to receive attention in the 2000s. Lawrence and Webster (2002) partitioned NPISO events into those that were (78%) and were not (22%) linked to the MJO and attributed NP in both types to surface frictional convergence into the ER wave low pressure anomaly. In their landmark study, Jiang et al. (2004) analyzed a two-dimensional 2.5-layer model to study NP. They used the f -plane approximation to exclude the Rossby wave emanation mechanism (Wang and Xie 1996) and focused on the basic-state shear effect. With this simplified framework, they demonstrated that north of $\sim 5^\circ\text{N}$ easterly shear alone can generate a barotropic vorticity anomaly north of convectively driven baroclinic divergence, which then induces boundary layer convergence. For regions closer to the equator, they hypothesized that boundary-layer moisture advection by either the mean or anomalous wind is responsible for NP. Drbohlav and Wang (2005) further demonstrated the role of vertical advection of mean easterly shear as a generation mechanism for north-of-convection barotropic vorticity, noting that NP does not require zonal propagation, such as the MJO, but does require easterly shear. Bellon and Sobel (2008)

studied the NPISO with an intermediate aquaplanet model and concluded that meridional advection of baroclinic vorticity anomalies by the mean meridional flow produces positive north-of-convection barotropic vorticity anomalies that drive boundary layer convergence. They also noted that surface heat fluxes associated with surface westerlies contribute to the instability of this mode. Boos and Kuang (2010) studied the NPISO in a zonally symmetric nonhydrostatic cloud-resolving model and concluded that the NP mode is accomplished via equatorial beta drift, with Ekman pumping into the drifting gyres enhancing low-level moisture anomalies. Kang et al. (2010) argued that the relationship between equatorial waves and the vertical wind shear mechanism of Jiang et al. (2004) cannot fully explain simulated northward propagation. Their modeling study suggests that north-of-convection low-level convergence is induced by a secondary meridional circulation that results from momentum mixing (convective momentum transports) in the presence of easterly shear.

Prior to the development of dynamic theories for NP, surface fluxes were recognized as a potential driver for the NPISO. Webster (1983) proposed that positive surface temperature anomalies over the Indian subcontinent and Southeast Asian peninsula could destabilize the low-level atmosphere ahead (north) of convection, causing new convection to form north of existing convection. Vecchi and Harrison (2002) analyzed air–sea coupling in their study of SST and precipitation anomalies in the Bay of Bengal (BoB), noting the presence of cold SST anomalies in the northern BoB ~ 10 days prior to monsoon break events. The case for air–sea interactions as a driver of the NPISO has been bolstered through coupled general circulation model experiments in which ocean coupling improved the NPISO over that seen in atmosphere-only simulations with the same model (Fu et al. 2003, 2007, 2008; Fu and Wang 2004a,b; Rajendran and Kitoh 2006; Roxy and Tanimoto 2007; Klingaman et al. 2008b; Weng and Yu 2010). Several of these studies conclude that warm SST anomalies north of convection destabilize the lower troposphere, favoring development of new convection north of existing convection. Recently, Klingaman et al. (2008a) demonstrated an improved monsoon simulation in the atmosphere-only Hadley Center Atmospheric Model (HadAM3) (Pope et al. 2000) and concluded that high-frequency SST fluctuations are critical to simulating the monsoon. SST anomalies and their associated gradients can generate boundary layer convergence (Lindzen and Nigam 1987) on seasonal time scales (Back and Bretherton 2009), and there is some evidence to suggest that this process also contributes to such convergence on intraseasonal time scales (Hsu and Li 2012).

The purpose of this study is to investigate the relative importance of several of the above-described northward propagation mechanisms in the real world and in the superparameterized Community Climate System Model (version 3, SP-CCSM). This work builds upon noteworthy studies by Chou and Hsueh (2010) and Ajayamohan et al. (2011). SP-CCSM and its uncoupled atmosphere-only configuration simulate many critical features of the summer and winter season ISO (Khairoutdinov et al. 2005, 2008; Benedict and Randall 2009, 2011; Stan et al. 2010; DeMott et al. 2011). Several questions motivate this work. First, to what extent are any of the proposed NP mechanisms evident in the observations and in SP-CCSM? Is the modeled NPISO governed by the same processes as found in nature? Do different NP mechanisms dominate various stages of the NPISO life cycle? In addition, we examine ISO and equatorial Rossby wave composites in an effort to better understand how these two modes interact to produce the complex intraseasonal monsoon evolution.

The paper is organized as follows: Methodology and datasets are described in section 2. Section 3 presents observed and simulated mean fields and variance fields pertaining to the NPISO and NP mechanisms. Composites of NP mechanisms and their relative association with NPISO convection are shown in section 4, and results are discussed in section 5. Section 6 summarizes.

2. Methodology and datasets

Compositing methods

Following the approach of several other studies (e.g., Fu et al. 2003; Kiladis et al. 2009), we use gridded filtered daily outgoing longwave radiation (OLR) data to construct composite life cycles of Asian summer monsoon (ASM) dynamic and thermodynamic fields and northward propagation mechanisms for 1) 20–60-day and 2) equatorial Rossby wave filtered OLR anomalies. Global OLR anomalies are computed by subtracting the OLR mean annual cycle (mean plus first three harmonics) at each grid point from the raw OLR time series. Composite life cycles are constructed by regressing unfiltered normalized anomaly fields (normalizing transforms all time series to have a mean of zero and a standard deviation of one) onto normalized filtered OLR anomalies at a geographic base point at lags -15 to $+15$ days, where the specific filtering applied to the base-point OLR anomaly is determined by the wave type of interest. For ER waves, OLR anomalies are decomposed into two-dimensional time–space spectra via a Fourier transform and an inverse transform is then applied to the Fourier coefficients bounded by frequencies corresponding to 10–35-day

periods, westward zonal wavenumbers 1–10, and 8-m and 90-m equivalent depth dispersion curves (i.e., Wheeler and Kiladis 1999). For the ISO, a 20–60-day bandpass filter is sufficient to extract the predominantly eastward-propagating ISO signal in both observational and model datasets (results are not sensitive to filtering windows up to 20–100 days). The ISO-filtered OLR base-point time series is obtained via a Lanczos filter with 201 weights.

Composites of each wave type were constructed at each of six different base points, shown in Fig. 1, which illustrates the ASM domain defined by the June–August (JJA) minus December–February (DJF) precipitation difference (Wang et al. 2009; Wu and Li 2009). The base points represent the three major regions of ASM precipitation (Indian Ocean, Bay of Bengal, and the South China Sea), as well as the southern “initiation” and northern maximum rainfall regions of the NPISO. For brevity, we only present results for two base points (5°N , 90°E and 5°N , 120°E), but we note that composite evolution for each wave type is nearly invariant across all analyzed base points.

Observed wave composites were constructed through a combination of observed and analyzed fields. Base point OLR time series were obtained from the NOAA daily mean OLR data (Liebmann and Smith 1996) for the years 1989–2010. Six-hourly analyzed dynamic and thermodynamic fields, including surface temperature over land, were obtained from the interim European Centre for Medium-Range Weather Forecasts Re-Analysis (ERA-Interim, herein called ERAI) dataset (Simmons et al. 2006) for the same time period and averaged to daily mean resolution. Over ocean regions, we also composited daily-resolution 3-day running mean remotely sensed sea surface temperature (SST) anomalies from the Tropical Rainfall Measuring Mission (TRMM) Microwave Imager (TMI) (Kummerow et al. 1998) for the years 1998–2010. The TMI SST data were combined with the land-based ERAI daily mean surface temperature to create a spatially continuous time series of surface temperature from 1998 to 2010. We also use precipitation data from the Global Precipitation Climatology Project (GPCP) (Huffman et al. 2001).

We compare the observed wave composites to those simulated by the SP-CCSM. The SP-CCSM represents a new approach to the representation of convective processes compared to models using traditional cumulus parameterization schemes. Whereas traditional schemes estimate convective temperature and moisture (and sometimes momentum) tendencies as a function of large-scale forcing, superparameterization generates convective tendencies by imposing the large-scale forcing of each GCM grid column onto a cloud-resolving model (CRM) embedded within that grid column. A separate CRM is integrated in each GCM grid column.

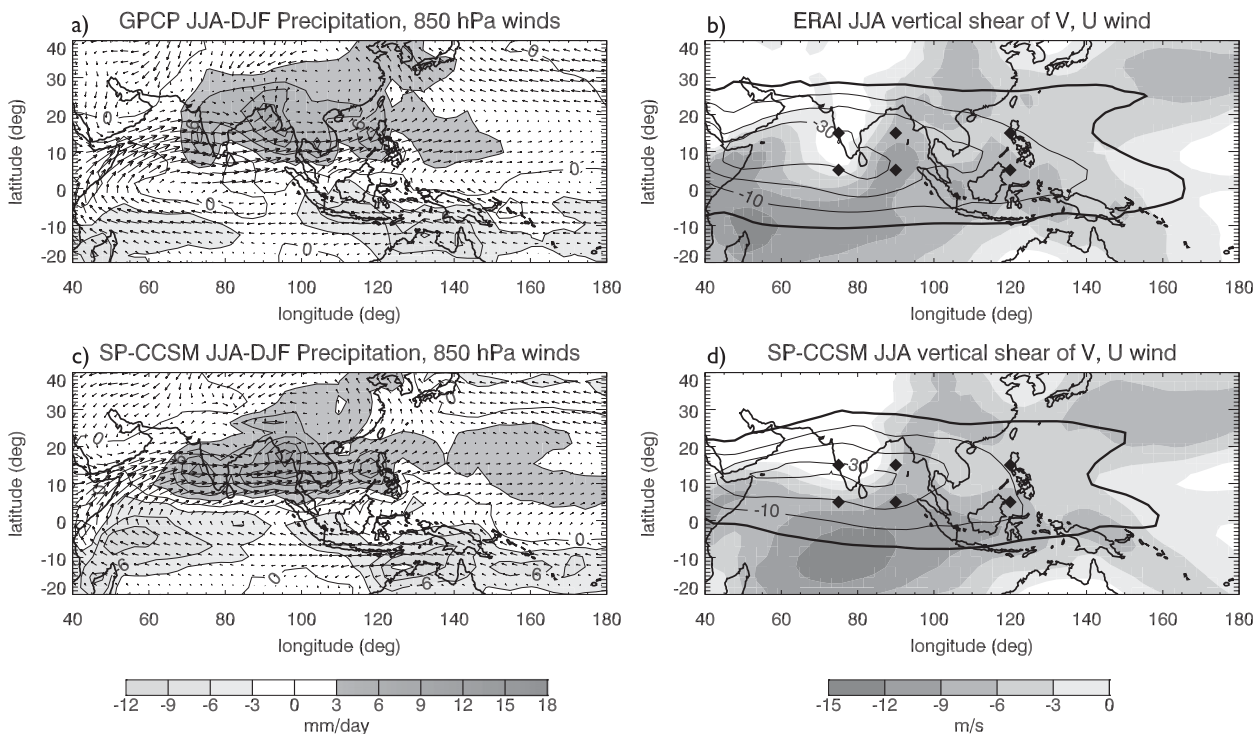


FIG. 1. (a) JJA – DJF observed mean 1989–2010 GPCP (Huffman et al. 2001) precipitation and ERAI 850-hPa winds and (b) observed JJA mean easterly shear ($U_{200} - U_{850}$; contour interval 10 m s^{-1}) and northerly shear ($V_{200} - V_{850}$; shaded). (c),(d) As in (a),(b), but for SP-CCSM. Black diamonds indicate compositing base points.

Details of SP-CAM, the atmosphere-only version of SP-CCSM, were discussed elsewhere (Khairoutdinov and Randall 2003; Khairoutdinov et al. 2005, 2008; DeMott et al. 2007, 2010), while Stan et al. (2010) and DeMott et al. (2011) described the behavior of SP-CCSM. Briefly, the CRM configuration is a two-dimensional, north–south oriented model with 4-km horizontal resolution and 30 vertical levels aligned with the GCM vertical grid spacing. The CRM runs continuously with a 20-s time step and receives forcing updates at the GCM 15-min time step, at which time convective temperature and moisture tendencies are provided to the GCM. Because of the two-dimensional CRM configuration, convective momentum tendencies are not passed to the GCM, so we are not able to address NPISO mechanisms linked to convective momentum transports (e.g., Kang et al. 2010).

3. Monsoon overview and variability of NP mechanisms

a. Monsoon overview

A thorough description of the monsoon in SP-CCSM can be found in DeMott et al. (2011). For background purposes, we present a limited summary of the monsoon in observations and in SP-CCSM.

JJA minus DJF mean fields for observations and SP-CCSM are shown in Figs. 1a and 1c. In observations, the Northern Hemisphere Asian summer monsoon region exhibits precipitation maxima near the west coast of India, the northern BoB, the Indo-China peninsula, and the western North Pacific (20° – 40° N), which is the East Asian summer monsoon (EASM) region (e.g., Wang et al. 2008). SP-CCSM produces the first three of these maxima, albeit with positive biases, and exhibits a broad negative bias in the EASM region. SP-CCSM does not adequately simulate the southern Indian Ocean zonally oriented precipitation band, but the simulated precipitation in that region is dominated by intraseasonal time scales (not shown). The 850-hPa winds in SP-CCSM agree well with observations, but are more zonal over the BoB than in observations. The JJA climatology of deep easterly (northerly) shear is shown in Figs. 1b and 1d, where easterly (northerly) shear is defined as negative values of the difference between 200- and 850-hPa zonal (meridional) winds. Easterly shear simulated by SP-CCSM agrees well with observations, although its magnitude and meridional extent is not as great over the western Indian Ocean as in observations. Northerly shear in SP-CCSM agrees well with observations everywhere except over the Arabian Sea, where it is deficient.

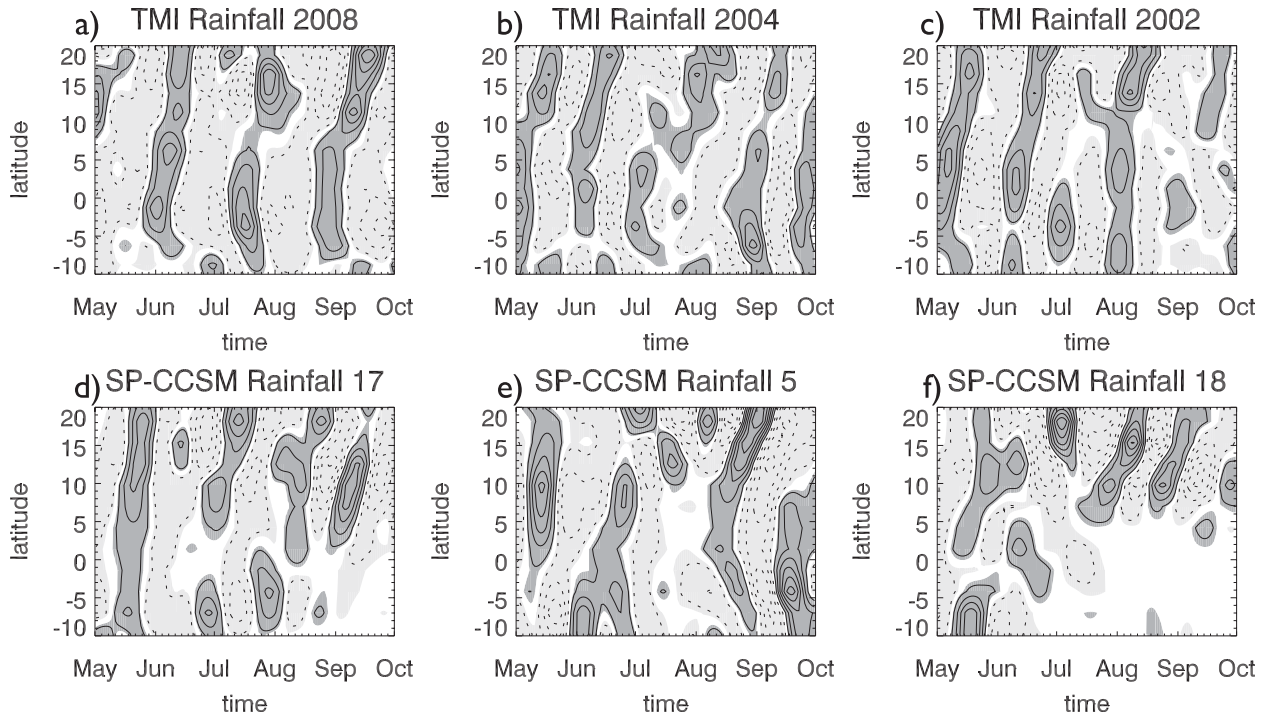


FIG. 2. May–October time–latitude cross sections of BoB (85° – 95° E average) 20–60-day filtered precipitation anomalies for (a)–(c) TRMM TMI and (d)–(f) SP-CCSM. Contour interval is 2 mm day^{-1} . Positive (negative) anomalies are dark (light) shaded.

The episodic nature of the NPISO over the BoB is illustrated in Fig. 2. Here, time series of 20–60-day filtered precipitation anomalies as a function of latitude are shown for three years of TMI precipitation data and three years of SP-CCSM data. The selected seasons were chosen to illustrate a variety of NPISO disturbances: events exhibiting robust, continuous northward propagation from the equator to $\sim 20^{\circ}$ N (TMI 2008; SP-CCSM May, year 17), the interaction of southward- and northward-propagating events (TMI July 2004; SP-CCSM July, year 5), and equatorial intraseasonal oscillation (ISO) events that do not result in NPISO events (TMI July 2002; SP-CCSM June, year 18).

b. Variability of NP mechanisms

The spatial inhomogeneity of quantities related to proposed NP mechanisms is demonstrated with maps of JJA variance of unfiltered fields in Figs. 3–5. Destabilization of the lower atmosphere by surface temperature (T_s) fluctuations (Figs. 3a,d) may be expected in regions where variances of lower tropospheric stability (LTS)—defined as $\theta_{700} - \theta_{1000}$, where θ is potential temperature; Figs. 3b,e—and T_s are both high. SP-CCSM LTS variance is greater than observed, but regional patterns of LTS variance are similar for both ERAI and SP-CCSM. Land-based LTS maxima are found over the eastern Arabian Peninsula, northern India, and eastern China; ocean-based maxima

are found over the northern Arabian Sea and equatorial Philippine Sea. The low variability of simulated SSTs may be a consequence of the coarse resolution ($\sim 3^{\circ}$) of the ocean model used in SP-CCSM. Overlapping areas of maximum observed T_s and LTS variance suggest that surface destabilization may be active in the following regions: the western Arabian Sea, the Philippine Sea, and northern India.

Boundary layer convergence forced by SST gradients may be expected in regions where the variance of the SST Laplacian is high (Figs. 3c,f) such as the northwest Pacific Ocean and western Arabian Sea in observations. Considerable model-to-observation differences are seen in the Indian Ocean, with SP-CCSM exhibiting stronger SST Laplacian variability in the eastern equatorial Indian Ocean than observations.

The easterly shear mechanism of Jiang et al. (2004) and the vorticity advection mechanism of Bellon and Sobel (2008) both produce barotropic vorticity anomalies that drive boundary layer convergence. Consequently, regions where the variance of both barotropic vorticity (ζ_+ , where ζ_+ is the mean column-integrated vorticity between 1000 and 200 hPa) and boundary layer convergence (DIV_{1000}) are high may lead to northward propagation via this mechanism. Whether the barotropic vorticity anomalies arise from easterly or northerly shear is explored further in section 4. The JJA variance of

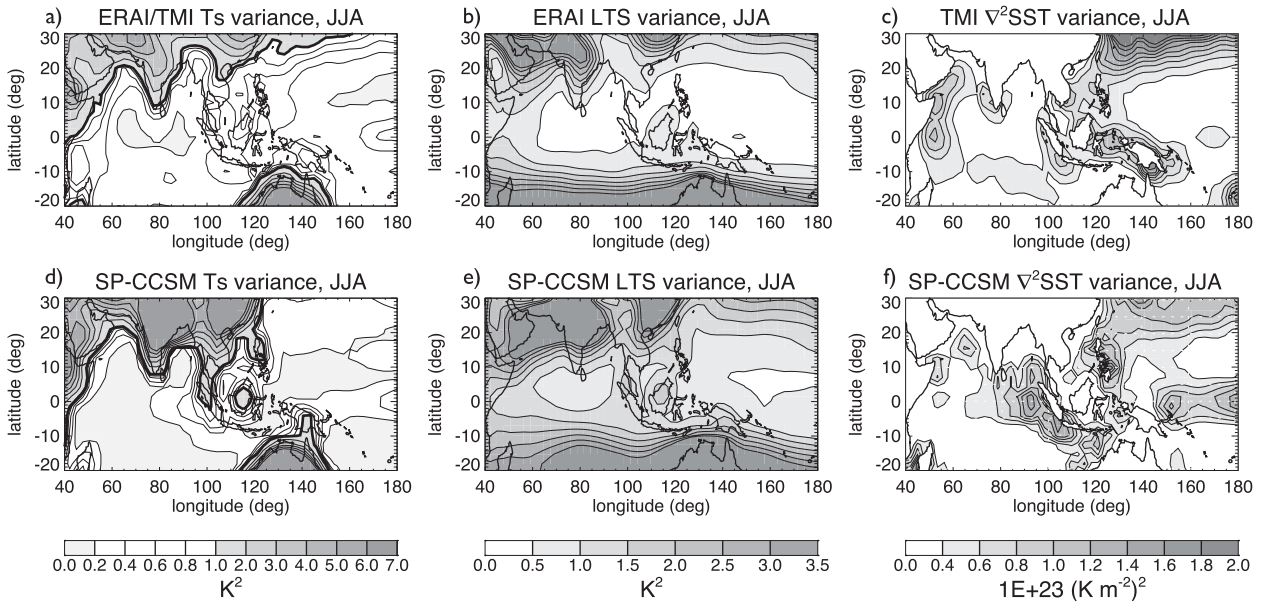


FIG. 3. ERAI and SP-CCSM JJA (a),(d) surface temperature variance, (b),(e) LTS variance, and (c),(f) SST Laplacian variance. In (a) and (c), surface temperature variance contour interval is 0.2 (1.0) K^2 for values less (greater) than 1, with values less than 0.2 K^2 shaded in light gray.

ζ_+ and 1000-hPa divergence for ERAI and SP-CCSM are shown in Fig. 4. In ERAI, two primary ζ_+ maxima are observed over the BoB and northwestern Pacific Ocean, with weaker variability found over the Arabian Sea and southern BoB. The two ζ_+ maxima are approximately collocated with DIV_{1000} variance maxima. In SP-CCSM, ζ_+ variance is concentrated over the northern BoB and

Bangladesh, and more broadly distributed over the northwestern Pacific Ocean. Boundary-layer divergence variance is larger in SP-CCSM than in the reanalysis product. The large simulated divergence is a consequence of the well-known tendency of superparameterization to produce stronger-than-observed tropical convection, while the low divergence variance in the reanalysis may arise

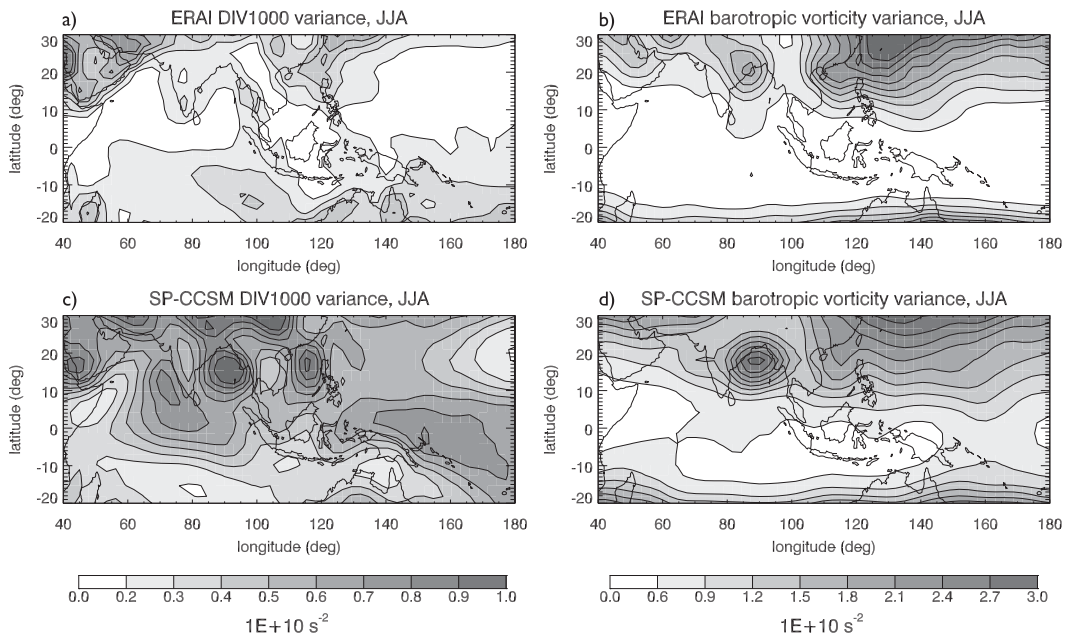


FIG. 4. ERAI and SP-CCSM JJA (a),(c) 1000-hPa divergence variance and (b),(d) barotropic vorticity variance.

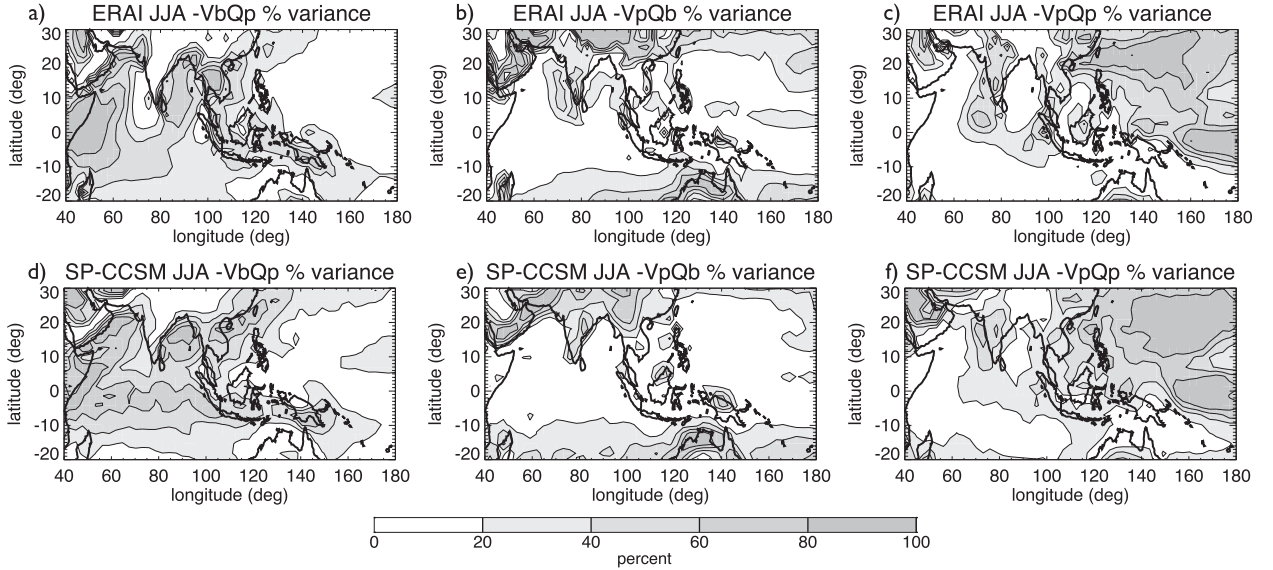


FIG. 5. Percentage of total JJA boundary layer (1000 hPa) meridional moisture advection by (a),(d) $-\bar{v}\delta q'/\delta y$, (b),(e) $-v'\delta\bar{q}/\delta y$, and (c),(f) $-v'\delta q'/\delta y$ in (top) ERAI and (bottom) SP-CCSM.

from low-level wind assimilation and/or extrapolating surface winds to below-ground pressures over land.

Northward propagation mechanisms associated with meridional advection of boundary layer moisture are illustrated in Fig. 5 with maps of the relative variance of each advective term (advection by mean and perturbation winds, as well as eddy flux terms) to the total variance. Although SP-CCSM absolute variance is greater than observed (not shown), there is good agreement with observations for the distribution of term-by-term relative variance. Observed meridional moisture advection is dominated by anomalous moisture advection by the mean meridional wind over most of the Indian Ocean (Figs. 5a,d). An exception is seen in the eastern Arabian Sea, where total advection is dominated by anomalous winds and eddy terms in ERAI (Figs. 5b,c). Eddy advection is largest in the west Pacific Ocean and eastern Arabian Sea (Fig. 5c). The largest difference between SP-CCSM and observations are found in the Arabian Sea, where the contribution of anomalous winds advecting mean moisture is deficient (Fig. 5e).

The above analysis suggests that any of the proposed NP mechanisms are likely to be active on a regional basis, rather than uniformly active over the entire ASM region. Consequently, northward propagation may be accomplished by different mechanisms depending on where the disturbance is located at a given time. Note that we have omitted the equatorial beta drift mechanism from our analysis, as its presence is difficult to evaluate using reanalyses or GCM output (Z. Kuang 2012, personal communication).

4. Relative contributions of NP mechanisms to northward propagation

a. Spatiotemporal evolution of NP mechanisms

Evaluating the relative importance of the above mechanisms in the NPISO is complicated by the different magnitudes of variability found in observations and SP-CCSM, the different quantities (with different units) being evaluated, and the need to somehow combine the effects of two different variables for some mechanisms (e.g., LTS and T_s for surface heating destabilization). We address these issues by constructing lag-regression composites: normalized time series (all time series have a mean of zero, and a standard deviation of one) of all NP-related fields are regressed onto normalized OLR anomalies at each of the six base points shown in Fig. 1. All coefficients are scaled by one negative OLR standard deviation (i.e., multiplied by -1). Local significance is assessed following Oort and Yienger (1996), with correlations greater than $r \sim 0.1$ being significant for the two-tailed 95% confidence interval. For mechanisms involving the combined, collocated effects of two different processes, the regression is performed separately for each normalized variable, and the appropriate-signed regression coefficients are averaged to provide a measure of the variance of that mechanism. Specifically, the index for the barotropic vorticity mechanism is the average of positive-only scaled ζ^+ regression coefficients and negative-only scaled 1000-hPa divergence coefficients (for convergence). For the surface heating destabilization mechanism, we average negative-only scaled LTS regression coefficients

(for reduced stability) and positive-only scaled T_s coefficients. The SST gradient mechanism index is the average of negative-only scaled SST Laplacian regression coefficients (Shimada and Minobe 2011) and negative-only scaled 1000-hPa divergence coefficients (for convergence).

The use of normalized time series and the linear combination of their regression coefficients allows us to qualitatively evaluate the relative variability of each NP mechanism in time and space and to compare disparate mechanisms that may be difficult to quantify. With this normalized perspective, the mechanism with the largest regression coefficient is assumed to be most strongly associated with NP. The disadvantage of this approach is the elimination of regional variability of any mechanism and the equalized contribution of variables that have the same units, but different magnitudes, such as the moisture advection terms shown in Fig. 5. It is important, therefore, to consider both the relative variance of any given mechanism and the spatial distribution and magnitude of its absolute variance. The standard disclaimer that “correlation is not necessarily causation” should also be considered when interpreting results; hence our preference for “association” rather than “causation.” Finally, our approach cannot adequately address cases where NP-linked variables are themselves correlated, indicating nonlinear processes. Sensitivity tests (not shown) indicate that JJA correlations among all possible NP-linked variable pairs in both observations and SP-CCSM are less than $r \sim 0.2$ over most of the domain. The exceptions are 1) moisture advection by mean and anomalous boundary layer winds and 2) boundary layer convergence and barotropic vorticity. The first is an example of possible nonlinearity, while the second supports the theory of barotropic vorticity driving boundary layer convergence.

Maps of ISO regression coefficients for each NP mechanism analyzed are shown in Fig. 6 at lag 0. Regression coefficients of terms associated with SST-linked mechanisms are shown in the top two panels, while dynamically linked terms are shown in the bottom two panels. The presence of large regression coefficients north of existing convection indicates that a mechanism may be active in promoting NP. Cold OLR anomalies (dark shading) in ERAI resemble convective anomalies associated with equatorially symmetric Rossby gyres. In SP-CCSM, the OLR signature is more zonally elongated, with a longitudinal offset in the Northern and Southern Hemisphere OLR minima. Surface temperature anomalies in ERAI/TMI (Fig. 6a) capture the distinct northwest–southeast tilted band of warm SSTs north of the convection, but these warm surface temperatures are only accompanied by negative LTS anomalies in the northern Arabian Sea

and northern India and Pakistan. The reason that large *normalized* SST deviations do not translate to similarly large normalized LTS deviations over most of the Indian Ocean is likely a consequence of the low *absolute* variability of SST in this region (see Fig. 3). The largest absolute SST variations in the Indian Ocean are observed over the northern and western Arabian Sea, and this is where strong local variations in normalized lower tropospheric stability (LTS) variability are also observed. At lag 0 days, coefficients for the negative Laplacian of SST (Figs. 6b,f) are found north of convection in the Indian and west Pacific Oceans in observations, but only over the Bay of Bengal in SP-CCSM.

Advection of boundary layer moisture (Figs. 6c,g) is concentrated along the northern boundary of anomalous ISO convection. Large coefficients are observed for advection by mean and anomalous winds, while eddy flux term coefficients (dashed lines) are small. Compared to the observations, SP-CCSM moisture advection is less closely associated with intraseasonal oscillation OLR anomalies than in observations. In observations and SP-CCSM, large coefficients of ζ_+ (Figs. 6d,h) lie on the northern boundary of Northern Hemisphere OLR anomalies. Boundary layer convergence is observed with and north of cold OLR anomalies in both reanalysis and model. In general, the SP-CCSM distribution of NP mechanisms agrees well with the reanalysis, but with somewhat smaller magnitudes and geographic extent. An exception is moisture advection by anomalous wind, which is not seen along either coast of India.

Our regression analysis cannot determine which of the analyzed mechanisms or combination of mechanisms is actually responsible for northward propagation, but it does allow us to qualitatively assess which mechanism exhibits the greatest variance associated with northward propagating convection, which we refer to as the leading mechanism. The picture that emerges from Fig. 6 is that, for both observations and SP-CCSM, multiple NP mechanisms are active north of ISO convective anomalies. Furthermore, for all lags, regression coefficients of different NP mechanisms tend to maximize in different regions. This is demonstrated in Fig. 7 with a latitudinal cross section of NP mechanism indices in the BoB. As convection migrates northward, the leading NP mechanism shifts from moisture advection by anomalous winds at lag -5 days to a combination of the barotropic vorticity and moisture advection mechanisms at lag $+5$ days, with smaller contributions from other mechanisms.

Leading mechanisms for the ISO composited at base point 5°N , 90°E at several lags are shown in Fig. 8. Leading mechanisms and anomalies of OLR and 850-hPa winds are only plotted where their regression coefficient is significant and exceeds $r = 0.1$. This criterion is satisfied

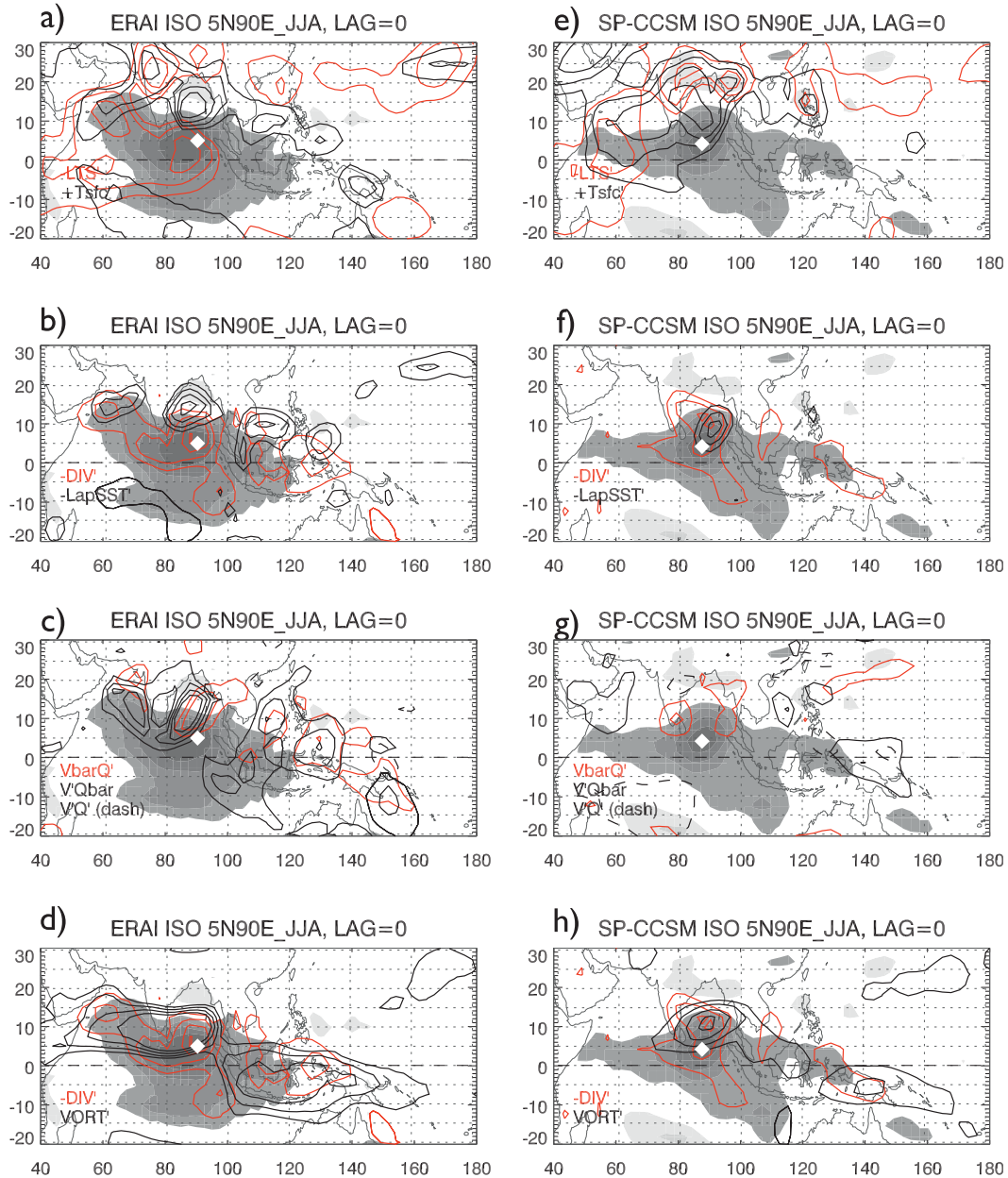


FIG. 6. Regression coefficients of NP-related normalized time series regressed onto the normalized 20–60-day OLR anomaly at 5°N, 90°E for (left) ERAI and (right) SP-CCSM. Black and red contour interval is 0.05 normalized units, starting with 0.1. OLR shading interval is 0.1 normalized units, starting with ± 0.1 . The mechanism being evaluated and its index definition are (a),(e) surface temperature destabilization, $[(T_{\text{sfc}} \geq 0.1) + (\text{LTS} \leq 0.1)] \times 0.5$; (b),(f) boundary layer convergence forced by SST gradients, $[(-\nabla^2 \text{SST} \geq 0.1) + (\text{DIV}_{1000} \leq 0.1)] \times 0.5$; (c),(g) boundary layer moisture advection, $-\bar{v}\delta q/\delta y \geq 0.1$, $-v'\delta\bar{q}/\delta y \geq 0.1$, and $-v'\delta q'/\delta y \geq 0.1$; and (d),(h) barotropic vorticity mechanism, $[(\zeta_+ \geq 0.1) + (\text{DIV}_{1000} \leq 0.1)] \times 0.5$.

at many points, but we are interested in those points that 1) lie north of existing convection and 2) result in a northward shift of convection at later lags. For ERAI (Figs. 8a–d), OLR anomalies exhibit an evolution consistent with the well-known progression of the ISO in JJA: equatorial convection in the Indian Ocean (Fig. 8a)

expands northward and southward as it propagates to the east (Fig. 8b), with the northern branch propagating farther poleward than the southern branch (Fig. 8c). The northward-propagating branch also exhibits a slow westward-moving component that, when combined with the eastward propagation over the Maritime Continent,

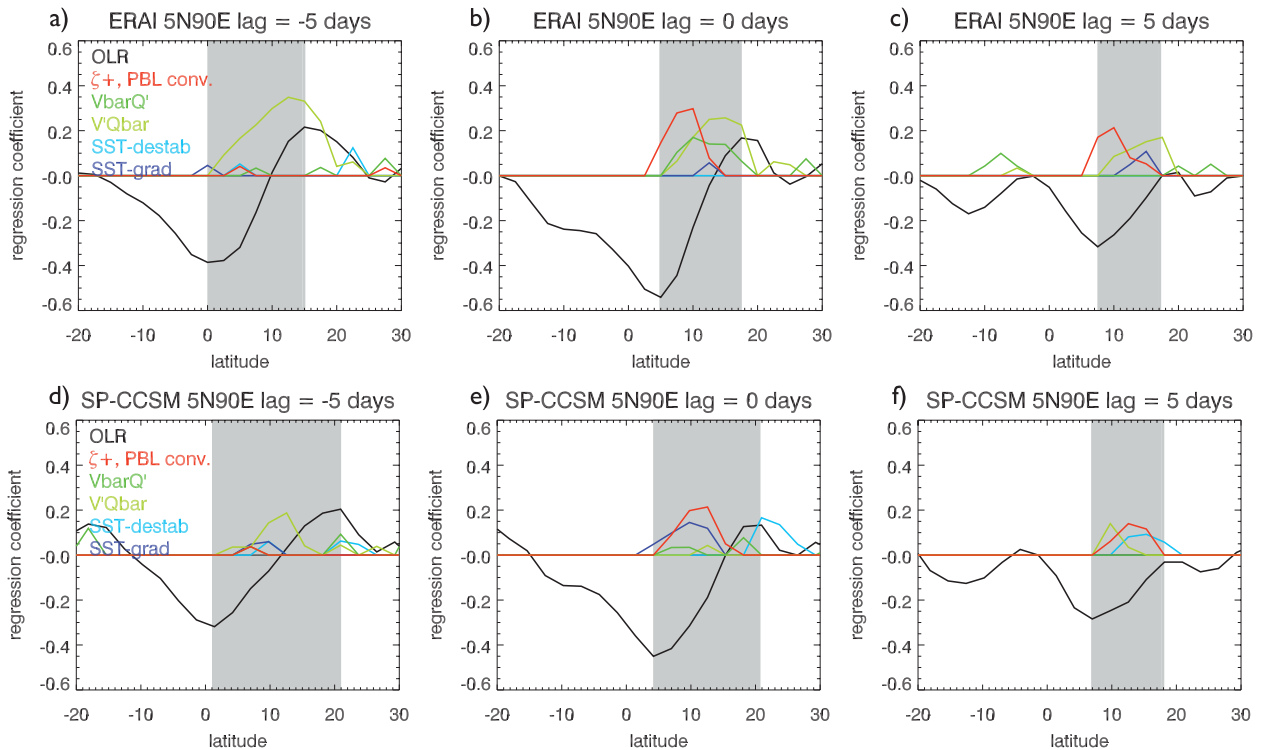


FIG. 7. Meridional cross section of ISO OLR and NP mechanism regression coefficients averaged from $90^{\circ} \pm 2.5^{\circ}\text{E}$ in (a)–(c) ERAI and (d)–(f) SP-CCSM for lag -5 , 0 , and $+5$ days: OLR (black), barotropic vorticity mechanism (red), $-\bar{v}\delta q/\delta y$ (dark green), $-v'\delta\bar{q}/\delta y$ (light green), surface temperature destabilization (light blue), and SST gradient mechanism (dark blue). Gray background shading highlights the region north of coldest composite OLR anomalies where NP mechanisms may influence future convective activity.

results in the northwest–southeast-tilted convective band (Fig. 8d).

During the ISO developing phase (Fig. 8a), boundary layer moisture advection by anomalous winds is the leading mechanism over most of the Indian Ocean with a few grid points dominated by the barotropic vorticity, surface temperature destabilization, and SST gradient mechanisms. As convection moves northward, the barotropic vorticity mechanism (red) assumes a larger role. This is consistent with the assertion of Jiang et al. (2004) that a mechanism other than easterly shear-produced barotropic vorticity must be active for convection centered near the equator since that mechanism can only operate north of $\sim 5^{\circ}\text{N}$. Surface temperature destabilization is the leading mechanism for a few points over the Arabian Sea (Fig. 8b).

Leading NP mechanisms for the ISO in SP-CCSM are shown in Figs. 8e–h. In the developing stage (Fig. 8e), boundary layer moisture advection by anomalous winds is again the leading mechanism. A notable difference between SP-CCSM and observations is seen at lag 0 days, where the simulated barotropic vorticity and moisture advection mechanisms, and the northward shift of convection, are largely absent over the Arabian Sea. It is not

until lag $+5$ days that SP-CCSM produces these two features. Consistent with observations, SST destabilization is apparent in the Arabian Sea at lag 0 days. The SP-CCSM tilted OLR band is not as distinct as it is in the NOAA OLR data, but its presence is more clearly seen in Fig. 10 of DeMott et al. (2011).

The 20–60-day filtering applied to the base-point OLR anomaly time series in Fig. 8 clearly captures the eastward-propagating MJO disturbance, but it also retains a portion of the power spectrum that includes equatorial Rossby waves, which are typically filtered to allow 10–35-day periodicities of westward-propagating waves. Since the northward propagation of the boreal summer ISO is generally understood to be the interaction of ER waves with deep easterly shear (e.g., Wang and Xie 1996), we examine leading NP mechanisms for the more constrained ER wave filtered base point at 5°N , 90°E in Fig. 9. The results reveal a complex sequence of ER propagation in the ERAI data (Figs. 9a–d). At lag -3 days (Fig. 9a), an elongated southwest–northeast-tilted cold OLR anomaly is observed. This OLR band extends beyond a similarly oriented open cyclonic vortex centered at $\sim 15^{\circ}\text{N}$, 105°E . The solid black arrow in Fig. 9a indicates the movement of the OLR anomaly from

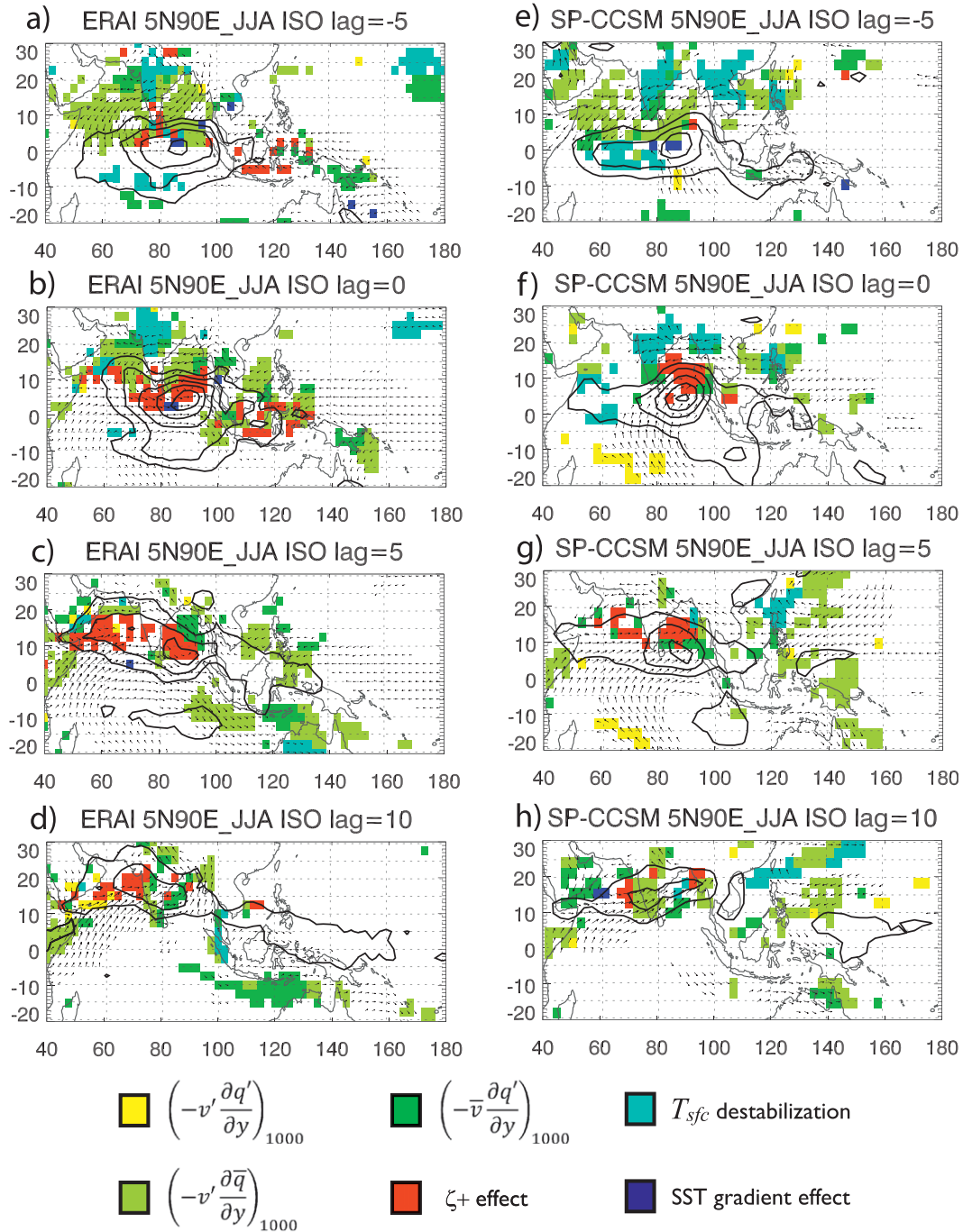


FIG. 8. Maps of leading NP mechanisms for 20–60-day filtered OLR anomalies at the 5°N, 90°E base point for (a)–(d) ERAI and (e)–(h) SP-CCSM at lag –5, 0, +5, and +10 days. Negative OLR regression coefficients are shown with black contours (contour interval is 0.1 standardized units) and 850-hPa zonal and meridional wind regressions (for $r \geq 0.1$) are indicated with vectors. Color coding in the legend is as in Fig. 7.

lags –10 to –4 days. Between lag –3 and lag 0 days, the OLR anomaly rapidly moves to the southwest, shown by the dashed black line. At lag 0 days (Fig. 9b), the Northern Hemisphere OLR anomaly is accompanied by a weaker Southern Hemisphere OLR anomaly, an arrangement

that is similar to the all-season ER wave composite in Fig. 17a of Kiladis et al. (2009). For lags of 3–6 days (Figs. 9c,d) the OLR anomaly once again travels in a northwestward direction. This “zigzag” westward movement of ER anomalies is observed for all base points at

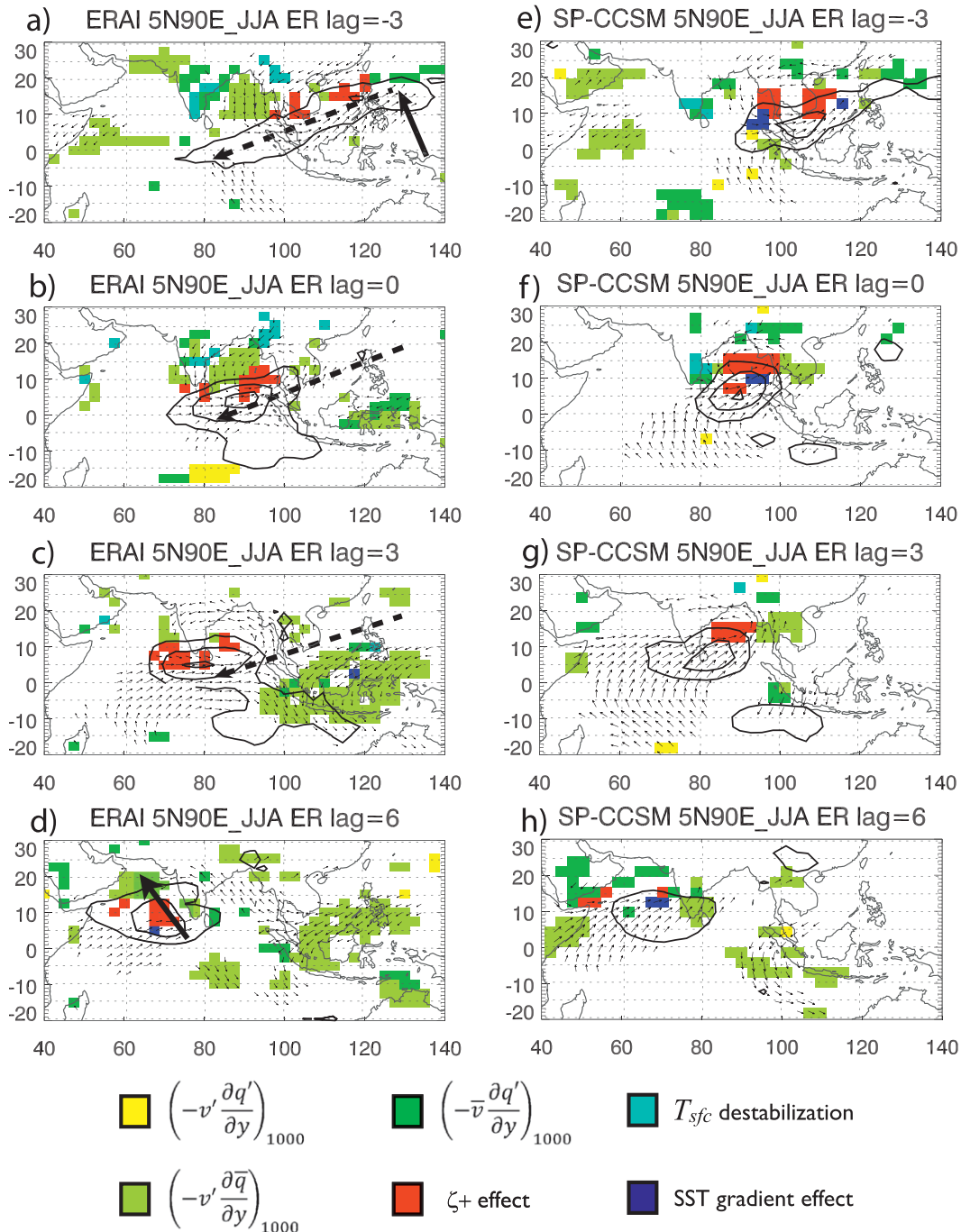


FIG. 9. As in Fig. 8, but for ER waves at the 5°N, 90°E base point and lags = -3, 0, +3, and +6 days. Solid black arrow in (a) indicates motion of OLR anomaly prior to lag -3 days. Dashed arrows in (b) and (c) indicate motion of OLR anomaly from lag -3 days through lag +6 days. Solid black arrow in (d) indicates motion of OLR anomaly after lag +6 days.

5°N. For 15°N base points, evidence of the zigzag pattern is evident but is also accompanied by purely westward-propagating disturbances centered at 15°N.

For equatorial Rossby (ER) waves, barotropic vorticity and boundary layer moisture advection are leading NP

mechanisms near the deepest convection. At lag 0 days, ER NP mechanisms (Fig. 9b) mirror ISO NP mechanisms in the BoB (Fig. 8b). Similarly, over the Arabian Sea and India Ocean in ERAI at lag +6 days, the ER low-level wind field (Fig. 9d) resembles a longitudinally stretched

cyclonic vortex, similar to that seen at lag +5 days for the ISO composite (Fig. 8c). This similarity in ER wave and ISO wind fields near the northern limit of the NPISO supports the conceptual model that the tilted ISO rainband is the result of ER waves interacting with vertical shear of environmental winds. These similarities are also present, although less clearly, in SP-CCSM. The fact that northward propagation is more evident at slower ISO time scales, rather than in the 10–35-day filtered ER wave composite, suggests that NP mechanisms have the greatest effect on the slowest ER waves.

Northward propagation mechanisms for the ISO composited about the 5°N, 120°E base point are shown in Fig. 10. For the ISO in the west Pacific Ocean (Figs. 10a–d), boundary layer moisture advection and the barotropic vorticity mechanism are also strongly associated with NP, and are observed both east and west of the Philippines. The SST gradient mechanism is also active at a few points, especially at later lags. In SP-CCSM (Figs. 10e–h), the barotropic vorticity mechanism is observed only west of the Philippines. This difference may account for the weaker simulated NP in this region. The ISO west Pacific OLR maximum that develops at lag –5 days in ERAI is accompanied by ER-wave-like low-level winds as it slowly propagates northwestward.

As noted earlier, a drawback to using normalized time series to study NP is the elimination of magnitude differences among variables with the same units and model-to-observation comparisons of single variables. Additional insight into NP is gained by studying composites that retain magnitude information via nonnormalized regressions. As an example, Fig. 11 illustrates the magnitude of several NP-linked variables for the ISO at lag –5 days, which corresponds to the time just before NP is observed over the Arabian Sea. Note that Arabian Sea $-\nabla^2\text{SST}$ is less in SP-CCSM than in observations, so this could be one cause of reduced NP in the model. However, the mechanism is active far north of observed convection (Fig. 11g), and further study is needed to determine if pressure gradients induced by SST gradients could have measurable impacts on free-tropospheric pressure gradients.

Perhaps more importantly, SP-CCSM simulates moisture advection and low-level destabilization equal to or larger than those seen in observations; yet SP-CCSM NP in the Arabian Sea is lacking (Fig. 8f). The only north-of-convection variable that is weaker than observed is barotropic vorticity, suggesting that this mechanism is critical to NP in this region: boundary layer convergence induced by the vorticity anomaly may serve as a “collector” of low-level moisture provided by moisture advection. Since SP-CCSM precipitation variability is quite large in the Arabian Sea (not shown), the weaker-than-observed

seasonal mean easterly shear in SP-CCSM (Fig. 1d) may be the root of weaker-than-observed NP in this region.

b. Barotropic vorticity and the role of zonal and meridional vertical wind shear

Up to now, we have not addressed how ζ_+ anomalies are generated, other than noting that they may be generated either by easterly shear of the mean zonal wind (Jiang et al. 2004) or northerly shear of the mean meridional wind (Bellon and Sobel 2008). The ζ_+ generation by easterly shear is accomplished as follows: low-level westerly winds and upper-level easterly winds generate a southward-pointing horizontal vorticity vector. Near-equatorial deep convection tilts the horizontal vorticity vortex tube, producing positive (negative) vertical ζ_+ anomalies north (south) of convection. Barotropic divergence associated with the ζ_+ anomaly induces boundary layer convergence, leading to the northward shift of convective activity. In the presence of purely baroclinic convection, generation of ζ_+ anomalies is described by Eq. (9) of Jiang et al. (2004): $\delta\zeta_+/\delta t \sim U_T\delta D_-/\delta y$, where U_T is the vertical shear of the mean zonal wind ($U_{200} - U_{850}$), and D_- is the anomalous baroclinic divergence, $(D_{-200} - D_{-850})/2$. The generation of ζ_+ by northerly shear is accomplished by the differential advection of baroclinic vorticity (ζ_-) anomalies by the mean meridional baroclinic wind. Convection generates low-level (upper level) positive (negative) vorticity anomalies, yielding a baroclinic vorticity couplet. Both low-level and upper-level environmental meridional winds acting on this ζ_- couplet result in positive (negative) vorticity advection north (south) of convection, leading to a positive (negative) ζ_+ anomaly north (south) of convection. This process is described in the first term of Eq. (36) of Bellon and Sobel (2008): $\delta\zeta_+/\delta t \sim -V_T\delta\zeta_-/\delta y$, where V_T is the vertical shear of the mean meridional baroclinic wind ($V_{-200} - V_{-850}$), and $\zeta_- = (\zeta_{-200} - \zeta_{-850})/2$.

The JJA variance of both $U_T\delta D_-/\delta y$ and $-V_T\delta\zeta_-/\delta y$, which we refer to as U_{gen} and V_{gen} , in ERAI and SP-CCSM are shown in Fig. 12. For both ERAI and SP-CCSM, U_{gen} maximizes in the Indian Ocean, whereas V_{gen} maximizes in the eastern BoB and the west Pacific. The relative magnitude of the two terms is shown in the bottom panels of Fig. 12 as the ratio $U_{\text{gen}}/V_{\text{gen}}$, emphasizing the dominance of U_{gen} over V_{gen} over much of the Asian summer monsoon region, but especially in the Indian Ocean. The spatial distribution of U_{gen} and V_{gen} variance is almost identical to the mean wind shear distributions shown in Fig. 1, suggesting that the mean wind field, and not the meridional gradient terms, is primary control for both of these mechanisms.

Despite the similar spatial structures of U_{gen} , V_{gen} , and their ratio, note that U_{gen} and V_{gen} in SP-CCSM are

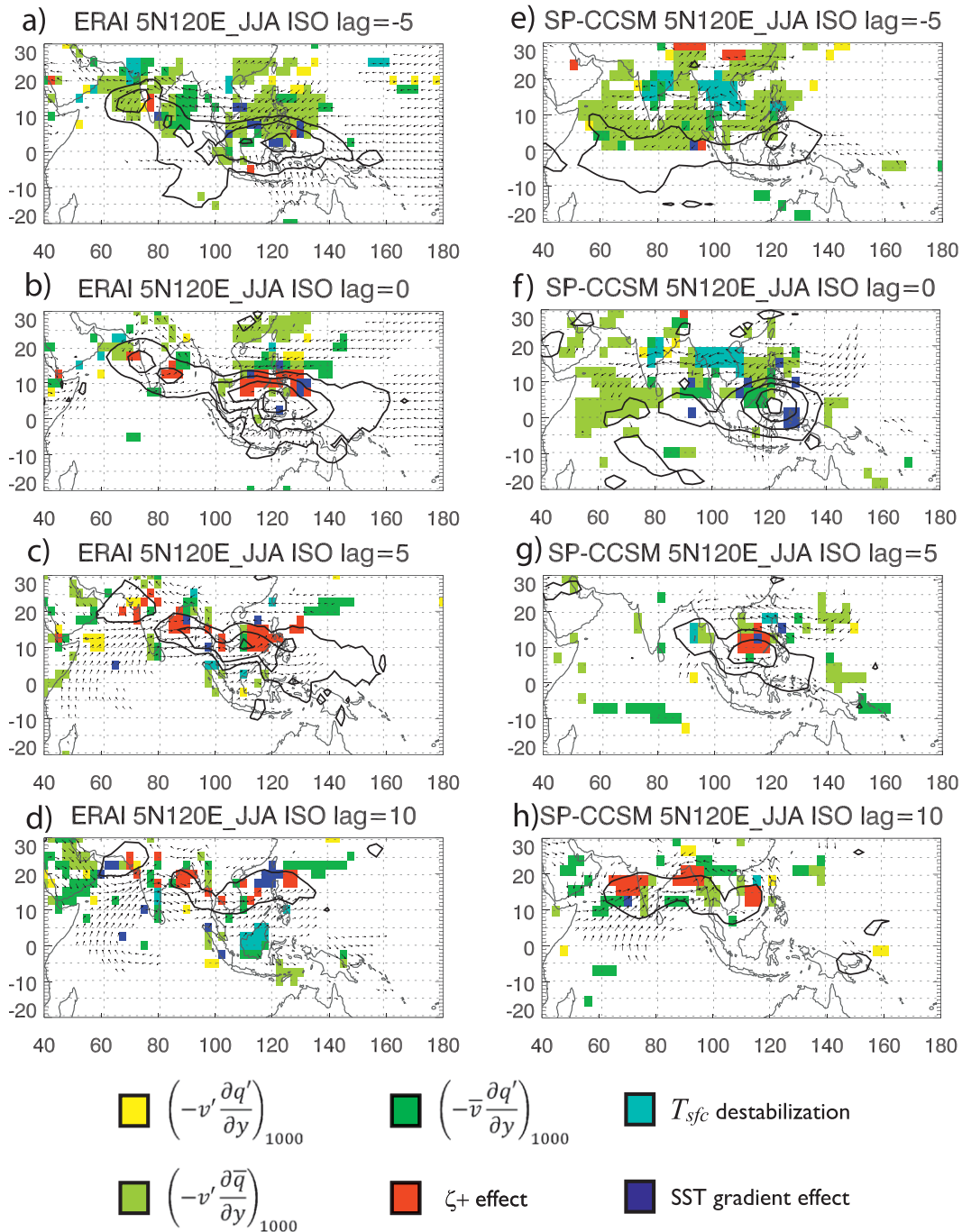


FIG. 10. As in Fig. 8, but for ISO activity at the 5°N, 120°E base point.

nearly an order of magnitude larger than in ERAI. Because the mean shear is nearly equal in SP-CCSM and observations, the difference must arise from a combination of the larger spatiotemporal variance of SP-CCSM convection and/or larger meridional gradients of these terms. This discrepancy in U_{gen} and V_{gen} magnitudes raises an interesting question: why is the barotropic vorticity

mechanism and northward propagation not more evident in the western Indian Ocean in the SP-CCSM ISO (Fig. 8f) given the higher ζ_{+} generation rates?

The meridional structure of ζ_{+} , U_{gen} , and V_{gen} for the BoB intraseasonal oscillation (Fig. 13) provides a clue. At lag -5 days, positive ζ_{+} anomalies are accompanied by positive U_{gen} anomalies at nearly all latitudes. Positive

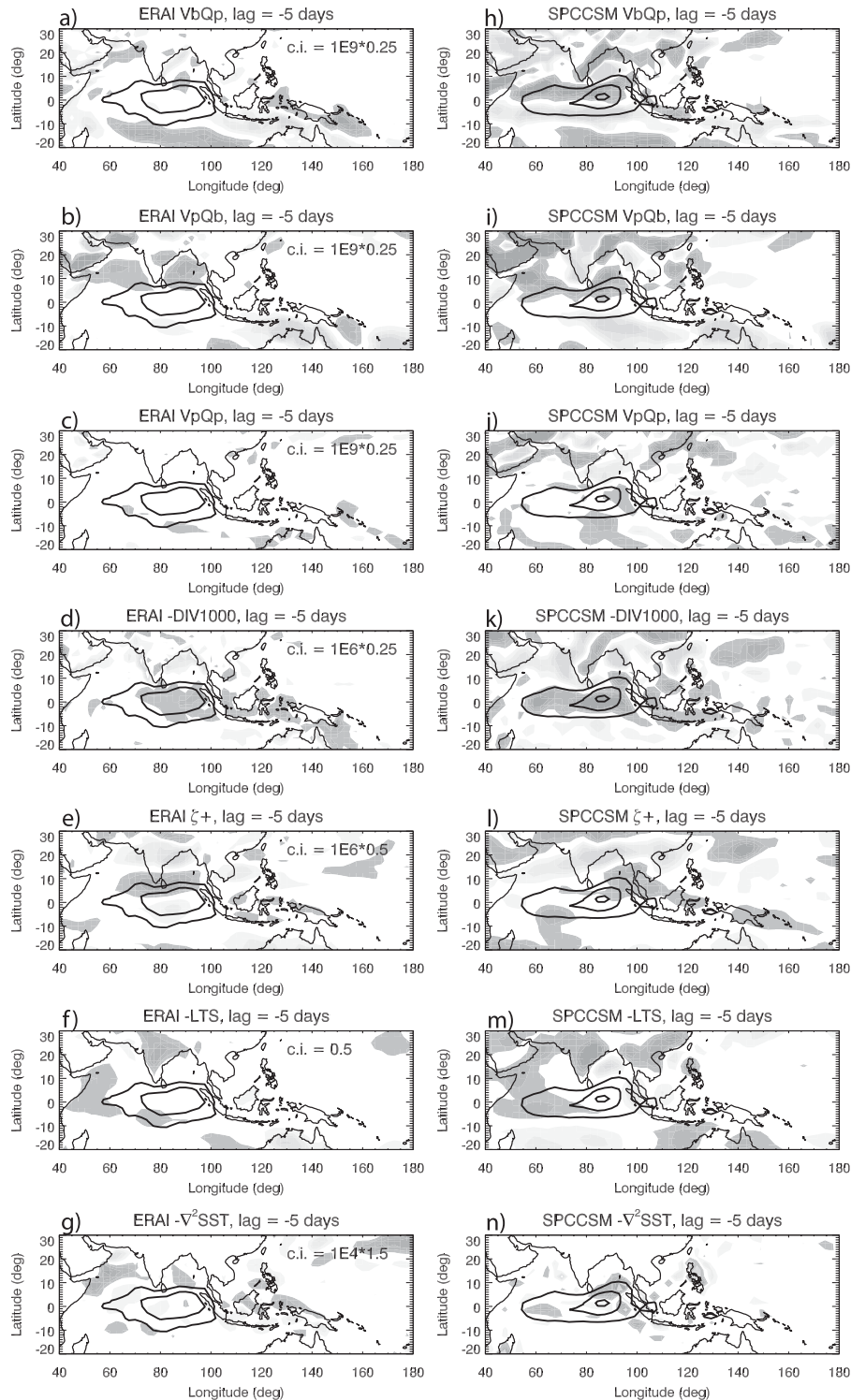


FIG. 11. Composite NP-linked variables at lag -5 days at the 5°N , 90°E base point: (a)–(c) and (h)–(j) moisture advection (s^{-1}); (d),(k) DIV_{1000} (s^{-1}); (e),(l) barotropic vorticity (s^{-1}); (f),(m) lower tropospheric stability (LTS) (K); (g),(n) $-\nabla^2\text{SST}$ (K m^{-2}). Unfiltered variables (including OLR) are regressed onto 20–60-day filtered OLR anomalies at the based point, then scaled by -20 W m^{-2} . Cold OLR anomalies are shown with black solid lines (-5 and -10 W m^{-2}), and NP-linked variables are indicated with shading. Shaded contour intervals are given in the left-hand panels and shading begins at ± 1 contour interval. Dark shading corresponds to positive NP in the Northern Hemisphere.

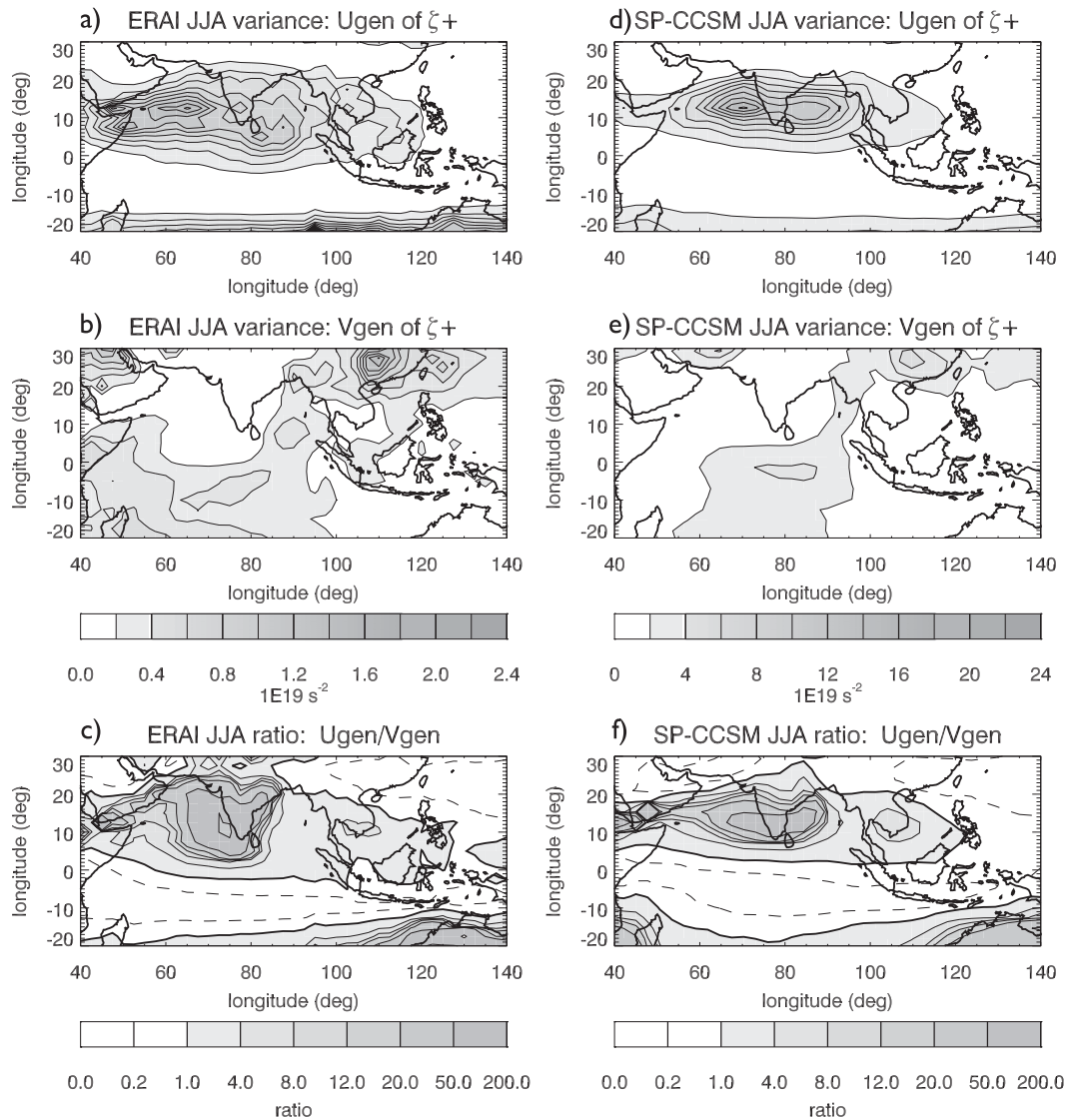


FIG. 12. Variance of JJA ζ_+ generation by (a),(d) zonal shear (U_{gen}) and (b),(e) meridional shear (V_{gen}), and (c),(f) the U_{gen}/V_{gen} ratio, in (left) ERAI and (right) SP-CCSM.

V_{gen} anomalies are also observed, but V_{gen} is also frequently *negative* when ζ_+ is *positive*. Therefore, V_{gen} may actually decrease ζ_+ anomalies in some regions while enhancing ζ_+ anomalies in others. A U_{gen} term that is several times larger than V_{gen} can more effectively offset the negative V_{gen} contributions, presumably leading to more effective northward propagation. Is a large U_{gen}/V_{gen} ratio, then, more favorable for NP than large U_{gen} or V_{gen} individually? The orientation of the U_{gen}/V_{gen} ratios shown in Fig. 12 is strikingly similar to the tilted rainband structures depicted by the OLR anomalies in Figs. 8 and 10 herein and in Fig. 10 of DeMott et al. (2011), raising the possibility that this ratio may be a key to the mean structure of monsoon rainfall.

5. Discussion

Our study examines normalized variability of several northward propagation mechanisms for the boreal summer intraseasonal oscillation and equatorial Rossby waves and finds that multiple NP mechanisms are active at any given time for both types of disturbances. For observed and modeled ISO composites, boundary layer moisture advection is the dominant mechanism when convection is located near the equator, while the barotropic vorticity and moisture advection mechanisms are more strongly associated with NP away from the equator. ER waves follow a circuitous path from the west Pacific to Indian Ocean, but their northward propagation is also associated

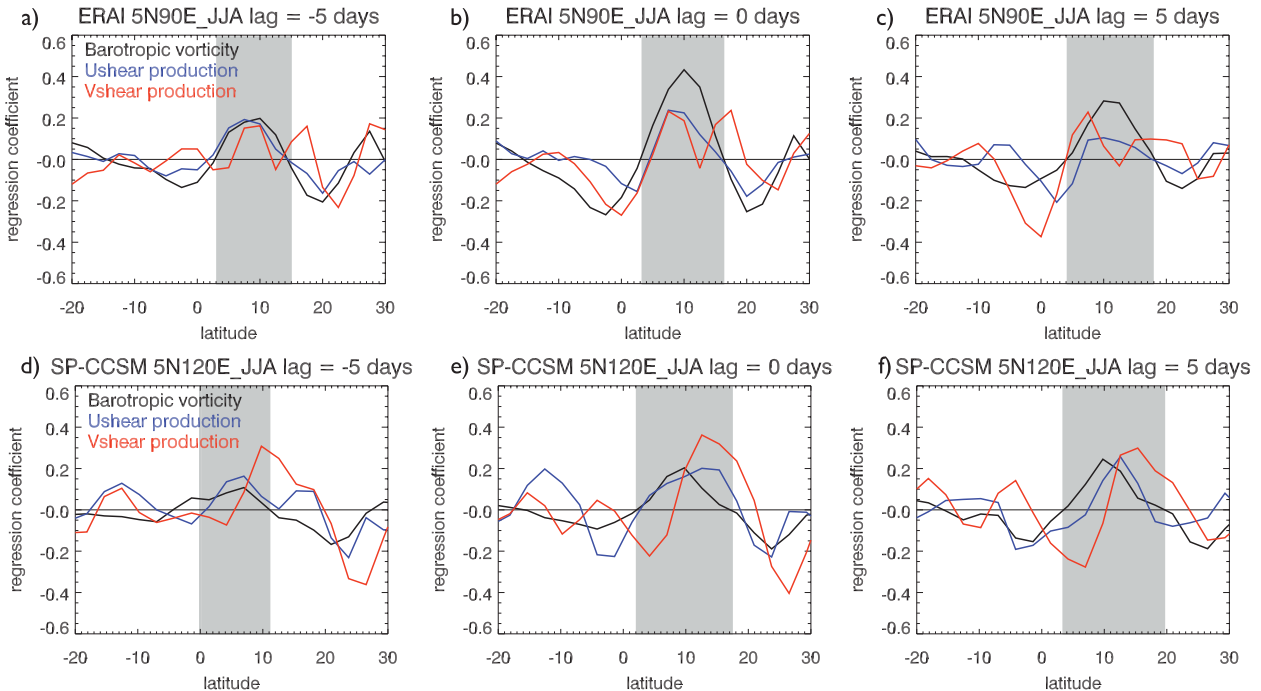


FIG. 13. Meridional cross section of ISO ζ_+ (black), U_{gen} (blue), and V_{gen} (red) regression coefficients averaged from $90^\circ \pm 2.5^\circ\text{E}$ in (a)–(c) ERAI and (d)–(f) SP-CCSM at lag -5 , 0 , and $+5$ days. Gray background shading highlights the region of Northern Hemisphere positive ζ_+ anomalies.

with the barotropic vorticity mechanism and moisture advection.

From the perspective of normalized time series, ISO moisture advection by anomalous winds exhibits greater variability than advection by mean winds, which is seemingly at odds with the conclusions of other studies (e.g., Chou and Hsueh 2010; Ajayamohan et al. 2011). This apparent discrepancy is reconciled, however, when the absolute variance of these two quantities and their spatial distributions are considered. For example, over the BoB at lag 0 days, scaling the normalized contours in Figs. 6c and 6d by the fractional contribution to total variance illustrated in Fig. 5, moisture advection by mean winds is about 30% larger than advection by anomalous winds in this region.

At ISO time scales, surface temperature destabilization is only evident over India and the northern Arabian Sea, despite large regions of positive SST anomalies ahead of northward-propagating convection (Fig. 3b). This is consistent with the observational analysis of Chou and Hsueh (2010) and the coupled modeling study of Ajayamohan et al. (2011) and suggests that intraseasonal SST anomalies are primarily symptomatic, rather than causative, of northward-propagating convection. Our results suggest that SST variability may play a larger role in NP by forcing low-level convergence anomalies (Lindzen and Nigam 1987; Back and Bretherton

2009), a conclusion that is consistent with the improved MJO forecast skill in coupled versus uncoupled models (Fu et al. 2008), although further study is needed to assess the strength of this mechanism. SST anomalies may also play an indirect role in the NPISO by modifying latent and sensible heat fluxes (Lestari et al. 2011; Chou and Hsueh 2010) or modulating the basic-state environment (Seo et al. 2007; DeMott et al. 2011).

The ISO composite is characterized by primarily MJO-like eastward-propagating OLR and wind anomalies on its eastern front. Within a few days of its arrival from the west, convection moves northward off the equator and the low-level winds acquire cyclonic rotation north of the convection. Animations of ISO composites at several base points reveal slow *westward* propagation of northward-drifting OLR anomalies embedded within the larger-scale northwest–southeast tilted convection band. This series of events supports the notion of the 40-day mode of the monsoon (Annamalai and Slingo 2001; Krishnamurthy and Shukla 2008) as the MJO excitation of equatorial Rossby waves, and the subsequent slowing and northward deflection of these waves as they interact with the environmental shear.

The ER wave composite is characterized by OLR anomalies originating in the west Pacific and propagating westward with a zigzag pattern: northwestward propagation in the west Pacific Ocean, southwest propagation

over the Maritime Continent, and northwestward propagation again in the Indian Ocean. Elements of this circuitous wave path can also be found in other studies that identify major oscillatory modes of the ASM. Annamalai and Slingo (2001) identified a 15-day mode (their Fig. 9) that closely resembles the lag 0 days ER wave composite shown in Fig. 9b. The southwestward propagation across the Maritime Continent, however, is more evident in their Fig. 7, which illustrates the temporal evolution of the 40-day mode. Krishnamurthy and Shukla (2008) identify 45- and 28-day oscillatory modes of the ASM. Evolution of the 28-day mode (their Fig. 5) reveals a west Pacific OLR anomaly at $\sim 15^{\circ}\text{N}$ interacting with an Indian Ocean eastward-moving equatorial OLR anomaly, giving the appearance of southwestward propagation into the Indian Ocean, which then propagates to the northwest. The intermingling of ER wave characteristics presented in our study with “fast” (e.g., 15 day), “intermediate” (e.g., 28 day), and “slow” (e.g., 40 day) modes of variability suggests that ER waves approaching the Maritime Continent interact with eastward-moving MJO disturbances approaching the Maritime Continent.

Figures 8–10 indicate that dynamic ERAI and SP-CCSM NP mechanisms are highly similar. At first glance, it is tempting to conclude that SP-CCSM is successful in simulating the BSISO because it correctly simulates the observed NP mechanisms. A key factor for most of the dynamic NP mechanisms is the effect of large-scale dynamics on boundary layer processes, particularly moisture convergence and/or advection. Successful simulation of the NPISO, then, appears to hinge upon the ability of convection—whether explicitly simulated or parameterized—to realistically respond to boundary layer changes. SP-CCSM is unique among current climate models in its representation of boundary layer processes, and especially the coupling of the boundary layer with deep convective clouds (Khairoutdinov and Randall 2003). This finescale, explicit interaction of convection with the boundary layer may allow convection simulated by SP-CCSM to respond to NP mechanisms in a more realistic manner than parameterized convection.

Our results emphasize the complex interactions between the basic-state tropical atmosphere, equatorial waves, and convection that produce the Asian summer monsoon. Successful simulation of the BSISO requires adequate representation of each of these elements, a point that was made by Sperber and Annamalai (2008), who noted that unstable coupled modes at intraseasonal time scales owe their existence to a favorable large-scale time-mean environment, atmospheric waves that are modified by the basic state, air–sea interaction, convection and water vapor feedbacks, and other factors. This stringent list of requirements for simulating the ASM highlights its

utility as a model diagnostic for GCM tropical weather simulation.

6. Summary

The role of several proposed mechanisms for the northward propagation of the ASM are examined in the ERA-Interim and in the superparameterized Community Climate System Model. Northward propagation mechanisms are evaluated by constructing normalized time series of indices related to each mechanism and compositing those indices about normalized filtered OLR anomalies at several base points throughout the Indian and west Pacific Oceans. Base point OLR anomalies are filtered for either intraseasonal or equatorial Rossby wave variability, which correspond to the two leading modes of boreal summer intraseasonal variability in this region. Lag-regression composites are constructed for each type of disturbance, and scaled for one standard deviation of the base point OLR time series, allowing direct comparison of the relative variability of each NP mechanism in space and time. Although this approach cannot identify the cause of NP, it does identify those mechanisms that are most associated with the northward shift of convection.

For both ISO (20–60 day) and equatorial Rossby wave filtering, there is widespread agreement between ERAI and SP-CCSM leading NP mechanisms, with multiple mechanisms observed north of convection at any given point and time. Eastward-moving intraseasonal oscillation convection in the Indian Ocean is centered on the equator and most strongly correlated with boundary layer moisture convergence. As ISO convection propagates northward, the interaction of convection with the mean state easterly and northerly shear induces anomalous barotropic vorticity north of convection, which generates boundary layer moisture convergence. Destabilization of the lower atmosphere by surface temperature anomalies are weakly associated with NP and only observed in the northern Arabian Sea and over the Indian subcontinent. Boundary layer convergence forced by SST gradients are more widespread, but of secondary importance to dynamic mechanisms.

We hypothesize that realistic simulation of NP mechanisms, which depend on a realistic basic state, is a necessary but not sufficient condition for simulating the northward propagation of the ASM. Rather, a realistic response of convection to boundary layer changes forced by these NP mechanisms, and subsequent interaction between convection and the environment are also required for a successful monsoon simulation.

Acknowledgments. This work received support from NSF Grant AGS-1119999, NOAA Grant NA09OAR431005,

NSF Grant 0830068, and NASA Grant NNX09AN50G. This work was also supported by the National Science Foundation Science and Technology Center for Multi-Scale Modeling of Atmospheric Processes, managed by Colorado State University under cooperative agreement ATM-0425247. We acknowledge the support of the Computational and Information Systems Laboratory at NCAR for providing computer time for this work.

REFERENCES

- Ajayamohan, R. S., H. Annamalai, J.-J. Luo, J. Hafner, and T. Yamagata, 2011: Poleward propagation of boreal summer intraseasonal oscillations in a coupled model: Role of internal processes. *Climate Dyn.*, **37**, 851–867.
- Annamalai, H., and J. M. Slingo, 2001: Active/break cycles: Diagnosis of the intraseasonal variability of the Asian summer monsoon. *Climate Dyn.*, **18**, 85–102.
- Back, L. E., and C. S. Bretherton, 2009: On the relationship between SST gradients, boundary layer winds, and convergence over the tropical oceans. *J. Climate*, **22**, 4182–4196.
- Bellon, G., and A. H. Sobel, 2008: Instability of the axisymmetric monsoon flow and intraseasonal oscillation. *J. Geophys. Res.*, **113**, D07108, doi:10.1029/2007JD009291.
- Benedict, J. J., and D. A. Randall, 2009: Structure of the Madden-Julian oscillation in the superparameterized CAM. *J. Atmos. Sci.*, **66**, 3277–3296.
- , and —, 2011: Impacts of idealized air–sea coupling on Madden-Julian oscillation structure in the superparameterized CAM. *J. Atmos. Sci.*, **68**, 1990–2008.
- Boos, W. R., and Z. Kuang, 2010: Mechanisms of poleward propagating, intraseasonal convective anomalies in cloud system-resolving models. *J. Atmos. Sci.*, **67**, 3673–3691.
- Chou, C., and Y.-C. Hsueh, 2010: Mechanisms of northward-propagating intraseasonal oscillation—A comparison between the Indian Ocean and the Western North Pacific. *J. Climate*, **23**, 6624–6640.
- DeMott, C. A., D. A. Randall, and M. Khairoutdinov, 2007: Convective precipitation variability as a tool for general circulation model analysis. *J. Climate*, **20**, 91–112.
- , —, and —, 2010: Implied ocean heat transports in the standard and superparameterized Community Atmospheric Models. *J. Climate*, **23**, 1908–1928.
- , C. Stan, D. A. Randall, J. L. Kinter, and M. Khairoutdinov, 2011: The Asian monsoon in the superparameterized CCSM and its relationship to tropical wave activity. *J. Climate*, **24**, 5134–5156.
- Drbohlav, H.-K. L., and B. Wang, 2005: Mechanism of the northward-propagating intraseasonal oscillation: Insights from a zonally symmetric model. *J. Climate*, **18**, 952–972.
- Fu, X., and B. Wang, 2004a: Differences of boreal summer intraseasonal oscillations simulated in an atmosphere–ocean coupled model and an atmosphere-only model. *J. Climate*, **17**, 1263–1271.
- , and —, 2004b: The boreal summer intraseasonal oscillations simulated in a hybrid coupled atmosphere–ocean model. *Mon. Wea. Rev.*, **132**, 2628–2649.
- , —, T. Li, and J. P. McCreary, 2003: Coupling between northward-propagating, intraseasonal oscillations and sea surface temperature in the Indian Ocean. *J. Atmos. Sci.*, **60**, 1733–1753.
- , —, D. E. Waliser, and L. Tao, 2007: Impact of atmosphere–ocean coupling on the predictability of monsoon intraseasonal oscillations. *J. Atmos. Sci.*, **64**, 157–174.
- , B. Yang, Q. Bao, and B. Wang, 2008: Sea surface temperature feedback extends the predictability of tropical intraseasonal oscillation. *Mon. Wea. Rev.*, **136**, 577–597.
- Hsu, P.-C., and T. Li, 2012: Role of the boundary layer moisture asymmetry in causing the eastward propagation of the Madden-Julian oscillation. *J. Climate*, **25**, 4914–4931.
- Huffman, G. J., R. F. Adler, M. Morrissey, D. T. Bolvin, S. Curtis, R. Joyce, B. McGavock, and J. Susskind, 2001: Global precipitation at one-degree daily resolution from multisatellite observations. *J. Hydrometeorol.*, **2**, 36–50.
- Jiang, X., T. Li, and B. Wang, 2004: Structures and mechanisms of the northward propagating boreal summer intraseasonal oscillation. *J. Climate*, **17**, 1022–1039.
- Kang, I.-S., D. Kim, and J.-S. Kug, 2010: Mechanism for northward propagation of boreal summer intraseasonal oscillation: Convective momentum transport. *Geophys. Res. Lett.*, **37**, L24804, doi:10.1029/2010GL045072.
- Khairoutdinov, M. F., and D. A. Randall, 2003: Cloud resolving modeling of the ARM summer 1997 IOP: Model formulation, results, uncertainties, and sensitivities. *J. Atmos. Sci.*, **60**, 607–625.
- , —, and C. DeMott, 2005: Simulations of the atmospheric general circulation using a cloud-resolving model as a superparameterization of physical processes. *J. Atmos. Sci.*, **62**, 2136–2154.
- , C. DeMott, and D. A. Randall, 2008: Evaluation of the simulated interannual and subseasonal variability in an AMIP-style simulation using the CSU Multiscale Modeling Framework. *J. Climate*, **21**, 413–431.
- Kiladis, G. N., M. C. Wheeler, P. T. Haertel, K. H. Straub, and P. E. Roundy, 2009: Convectively coupled equatorial waves. *Rev. Geophys.*, **47**, RG2003, doi:10.1029/2008RG000266.
- Klingaman, N. P., H. Weller, J. M. Slingo, and P. M. Inness, 2008a: The intraseasonal variability of the Indian summer monsoon using TMI sea surface temperatures and ECMWF reanalysis. *J. Climate*, **21**, 2519–2539.
- , P. M. Inness, H. Weller, and J. M. Slingo, 2008b: The importance of high-frequency sea surface temperature variability to the intraseasonal oscillation of Indian monsoon rainfall. *J. Climate*, **21**, 6119–6140.
- Krishnamurthy, V., and J. Shukla, 2008: Seasonal persistence and propagation of intraseasonal patterns over the Indian monsoon region. *Climate Dyn.*, **30**, 353–369.
- Kummerow, C., W. Barnes, T. Kozu, J. Shiue, and J. Simpson, 1998: The Tropical Rainfall Measuring Mission (TRMM) sensor package. *J. Atmos. Oceanic Technol.*, **15**, 809–817.
- Lau, K. M., and L. Peng, 1990: Origin of low-frequency (intraseasonal) oscillation in the tropical atmosphere. Part III. Monsoon dynamics. *J. Atmos. Sci.*, **47**, 1443–1462.
- Lawrence, D. M., and P. J. Webster, 2002: The boreal summer intraseasonal oscillation: Relationship between northward and eastward movement of convection. *J. Atmos. Sci.*, **59**, 1593–1606.
- Lestari, R. K., M. Watanabe, and M. Kimoto, 2011: Role of air–sea coupling in the interannual variability of the South China Sea summer monsoon. *J. Meteor. Soc. Japan*, **89A**, 283–290.
- Liebmann, B., and C. A. Smith, 1996: Description of a complete (interpolated) outgoing longwave radiation dataset. *Bull. Amer. Meteor. Soc.*, **77**, 1275–1277.
- Lindzen, R. S., and S. Nigam, 1987: On the role of sea surface temperature gradients in forcing low-level winds and convergence in the tropics. *J. Atmos. Sci.*, **44**, 2418–2436.

- Madden, R. A., and P. R. Julian, 1971: Detection of a 40-50 day oscillation in zonal wind in the tropical Pacific. *J. Atmos. Sci.*, **28**, 702–708.
- , and —, 1972: Description of global-scale circulation cells in tropics with a 40-50 day period. *J. Atmos. Sci.*, **29**, 1109–1123.
- Oort, A. H., and J. J. Yienger, 1996: Observed interannual variability in the Hadley circulation and its connection to ENSO. *J. Climate*, **9**, 2751–2767.
- Pope, V. D., M. L. Gallani, P. R. Rowntree, and R. A. Stratton, 2000: The impact of new physical parametrizations in the Hadley Centre climate model—HadAM3. *Climate Dyn.*, **16**, 123–146.
- Rajendran, K., and A. Kitoh, 2006: Modulation of tropical intraseasonal oscillations by ocean–atmosphere coupling. *J. Climate*, **19**, 366–391.
- Roxy, M., and Y. Tanimoto, 2007: Role of SST over the Indian Ocean in influencing the intraseasonal variability of the Indian summer monsoon. *J. Meteor. Soc. Japan*, **85**, 349–358.
- Seo, K.-H., J.-K. E. Schemm, W. Wang, and A. Kumar, 2007: The boreal summer intraseasonal oscillation simulated in the NCEP Climate Forecast System: The effect of sea surface temperature. *Mon. Wea. Rev.*, **135**, 1807–1827.
- Shimada, T., and S. Minobe, 2011: Global analysis of the pressure adjustment mechanism over sea surface temperature fronts using AIRS/Aqua data. *Geophys. Res. Lett.*, **38**, L06704, doi:10.1029/2010GL046625.
- Simmons, A., S. Uppala, D. Dee, and S. Kobayashi, 2006: ERA-Interim: New ECMWF reanalysis products from 1989 onwards. *ECMWF Newsletter*, No. 110, ECMWF, Reading, United Kingdom, 26–35.
- Sperber, K. R., and H. Annamalai, 2008: Coupled model simulations of boreal summer intraseasonal (30-50 day) variability, Part 1: Systematic errors and caution on use of metrics. *Climate Dyn.*, **31**, 345–372.
- Stan, C., M. Khairoutdinov, C. A. DeMott, V. Krishnamurthy, D. M. Straus, D. A. Randall, J. L. Kinter III, and J. Shukla, 2010: An ocean–atmosphere climate simulation with an embedded cloud resolving model. *Geophys. Res. Lett.*, **37**, L01702, doi:10.1029/2009GL040822.
- Vecchi, G. A., and D. E. Harrison, 2002: Monsoon breaks and subseasonal sea surface temperature variability in the Bay of Bengal. *J. Climate*, **15**, 1485–1493.
- Wang, B., and H. Rui, 1990: Synoptic climatology of transient tropical intraseasonal convection anomalies: 1975–1985. *Meteor. Atmos. Phys.*, **44**, 43–61.
- , and X. Xie, 1996: Low-frequency equatorial waves in vertically sheared zonal flow. 1. Stable waves. *J. Atmos. Sci.*, **53**, 449–467.
- , and —, 1997: A model for the boreal summer intraseasonal oscillation. *J. Atmos. Sci.*, **54**, 72–86.
- , Z. Wu, J. Li, J. Liu, C.-P. Chang, Y. Ding, and G. Wu, 2008: How to measure the strength of the East Asian summer monsoon. *J. Climate*, **17**, 4449–4462.
- , F. Huang, Z. Wu, J. Yang, X. Fu, and K. Kikuchi, 2009: Multi-scale climate variability of the South China Sea monsoon: A review. *Dyn. Atmos. Oceans*, **47**, 15–37.
- Webster, P. J., 1983: Mechanisms of monsoon low-frequency variability: Surface hydrological effects. *J. Atmos. Sci.*, **40**, 2110–2124.
- Weng, S. P., and J.-Y. Yu, 2010: A CGCM study on the northward propagation of tropical intraseasonal oscillation over the Asian summer monsoon regions. *Terr. Atmos. Oceanic Sci.*, **21**, 299–312.
- Wheeler, M., and G. N. Kiladis, 1999: Convectively coupled equatorial waves: Analysis of clouds and temperature in the wavenumber–frequency domain. *J. Atmos. Sci.*, **56**, 374–399.
- Wu, Z., and J. Li, 2009: Seasonal prediction of the global precipitation annual modes with the Gridpoint Atmospheric Model of IAP LASC (GAMIL). *Acta Meteor. Sin.*, **23**, 428–437.
- Xie, X., and B. Wang, 1996: Low-frequency equatorial waves in vertically sheared zonal flow. Part II: Unstable waves. *J. Atmos. Sci.*, **53**, 3589–3605.
- Zhang, C., 2005: Madden-Julian oscillation. *Rev. Geophys.*, **43**, RG2003, doi:10.1029/2004RG000158.